SHORT-TERM FORECASTING OF SOLAR RADIATION BASED ON SATELLITE DATA WITH STATISTICAL METHODS

Annette Hammer, Detlev Heinemann, Elke Lorenz, and Bertram Lückehe
Department of Energy and Semiconductor Research, Faculty of Physics, University of Oldenburg,
D-26111 Oldenburg, Germany, Telephone +49-441-798-3545, Fax +49-441-798-3326, E-mail elke.lorenz@uni-oldenburg.de

Abstract – This paper describes the various paper size and formatting requirements of paper submitted for the General Proceedings of the ISES 1999 Solar World Congress. This portion of the paper is the abstract. The abstract should not exceed 250 words, and should be complete in itself. It should summarise the conclusions of the paper as well as the methods used. Do not make reference citations in the abstract. The abstract is not to be considered as part of the introduction of the paper. It should be indented 7.5 mm left and right from the standard text border as defined below. Typeface should be set to Times Roman 9 pt. The abstract is characterised by the word "Abstract" in bold at the beginning of the paragraph, followed by a dash, not bold, between two spaces. The abstract should consist of only one paragraph. It is separated from the Author information by one blank line, and from the paper body by two blank lines.

1. INTRODUCTION

Fluctuations of solar irradiance are known to have a significant influence on electric power generation by solar energy systems. To ensure an efficient use of the solar resource this behaviour has to be considered in operating strategies for this systems. Depending on the application, prediction of solar irradiance is beneficial on different time scales from less then one hour up to several days[1]. Examples are the optimisation of the storage management in stand alone systems, power management of solar thermal plants or the control of electricity grids with high photovoltaic penetration rates.

For daily horizons forecast, routines based on the output of numerical weather prediction models have been developed in [2]. For a short range prediction, statistical models based on the ground measurements of the radiation show only limited accuracy [3] due to the lack of spatial information about the cloud situation. As cloudiness is the most important parameter governing the insolation, forecasting of solar radiation makes the description of development of the cloud situation an essential task.

Satellite data can provide information about cloudiness (and thus also about irradiance) with a high spatial (2.5km x 2.5km) and temporal (30 min) resolution. Thus satellite data should be an appropriate data base for forecasting irradiance.

Sequences of satellite cloud images will be used to extract information about motion, formation and dissolution of clouds. Assuming that for small scales the variability of the irradiance is mainly caused by the spatial drift of cloud structures, methods of image processing for detection of motion can be applied.

For this date several approaches have been proposed. The Maximum Cross Correlation has been used to determine the movement of cloud structures by Beyer et al [4]. Bahner et al. applied a functional analytic methods to derive displacement vector fields from satellite image sequences[5], and Cote and Tatnall developed a neural network based methods for tracking features from satellite images[6].

The purpose of this paper is to present a statistical method to calculate motion vector fields, based on an approach for the estimation of motion developed by Konrad and Dubois[7], which performes with very good accuracy and furthermore has the advantage of short computing times, what is also an essential point when calculating short range forecasts. The motion vector fields are applied on the present image to predict the future cloud situation and irradiance.

In our paper we will first describe the method to calculate cloud images from satellite images and how to derive the ground irradiance thereof . In section 3 the model we use to derive the motion vector fields is . Finally results will be presented and discussed with respect to accuracy and potential for solar energy applications

2. SATELLITE DATA

2.1 *METEOSAT satellite*

Images in the visible range of the geostationary satellite METEOSAT are used as a database for the forecast. The satellite takes images of the full earth disk every 30 minutes.

In the subsatellite point the spatial resolution is 2.5 km x 2.5 km, in central Europe approximately 2.5 km x 4.5 km. The data is provided as greyscale pixel images each pixel representing the radiance signal of solar radiation bckscattered to space by earth, atmosphere and clouds.

2.2 *HELIOSAT method to calculate cloud and radiation maps*

To derive the ground irradiance from satellite measurements we use an enhanced version of the semi-empirical HELIOSAT method [8].

In a first step an offset is subtracted from the satellite signal. From this corrected signal we calculate the relative reflectivity ρ by applying a normalisation with respect to solar elevation.

In a second step the degree of cloudiness, the cloudindex *n*, is derived from the relative reflectivity for each pixel with following model:

Depending on the amount of clouds, a part of the solar radiation, defined as cloud index *n*, is reflected by clouds with a high reflectivity ρ_{cl}, the other part is reflected by the ground with a low reflectivity ρ_{gr} (see Fig 1):

$$\rho = n\rho_{cl} + (n-1)\rho_{gr} \quad (1)$$

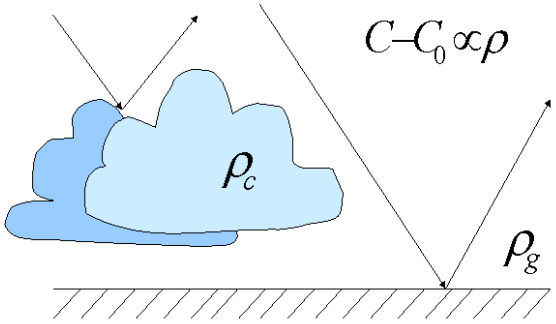

Fig. 1. Reflection of solar radiation from clouds and ground.

From the satellite images we can estimate a constant value for the cloud reflectivity ρ_{cl} and derive monthly maps for the ground albedo ρ_{gr}. Now it is possible to determine *n* using Equation (1):

$$n = (\rho - \rho_{gr})/(\rho_{cl} - \rho_{gr}) \quad (2)$$

The HELIOSAT method assumes a linear relationship between the cloud index n and the transmission through the atmosphere k^*, defined as ratio of surface global irradiance *G* to the clear sky irradiance G_{clear}.

$$k^* \equiv G / G_{clear} = 1 - n \quad (3)$$

The global irradiance G thus can be calculated directly from k^* using a clearsky irradiance model.
The error of the satellite retrieved irradiance estimated by comparison with half hourly mean values of ground measurements is about 20%, mean hourly values have an error of about 15%.

2.3. *Cloud images*

As stated in the introduction and quantified in Eqn. (3) cloudiness is the essential parameter for the insolation. Thus forecasts of values of the cloud index *n* can be used to determine the future irradiance applying Eqn. (3).
The advantage of using cloud index images instead of radiation maps is, that the daily pattern of radiation is not included. Thus we can just focus on determining the development of the clouds, the known information about the daily development of irradiance is added later.
An example for two consecutive cloudindex images is given in Fig 2. Cloud structeres are similar in both pictures. Small scale variations are not stable from one image to the next and change randomly. Filtering this ´noise´ improves the quality of the forecast considerably.

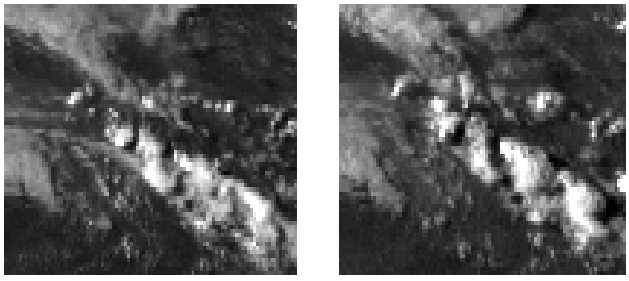

Fig. 2. Consecutive cloud index images of Northern Germany.

3. MOTION VECTOR FIELDS

From two consecutive images the motion of cloud structures shall be determined. To find a vector field that describes the true motion in the best way, we use a statistical approach based on a model developed by Konrad an Dubois [8]. The main ideas of this approach will be described in this section. The first step is to find an estimation criterion for the quality of a vector field. Then a model of motion is formulated described by a probability function. Finally the maximum of the probability is searched using a Monte Carlo Method.

3.1. *Terminology*

The true underlying image, in our case the real cloud situation, is denoted by u. The observed image g (the cloud index image measured by the satellite) is assumed to be a realisation of a random field G, while the displacement vector field d is considered to be a sample of a Random Vector Field D.

3.2. *Estimation criterion*

A maximum a posteriori probability criterion is used to estimate the most likely displacement field. The ´best´ motion vector field must satisfy the relation:

$$P(D = d^* \mid g_0, g_1) \geq P(D = d \mid g_0.g_1) \forall d \in D \quad (4)$$

where P is the conditional probability for a certain vector field, given two images g_0 and g_1. To calculate this probability, the Bayes rule for random variables is applied:

$$P(D = d \mid g_0, g_1) = \frac{P(G_1 = g_1 \mid d, g_0) P(d \mid g_0)}{P(G_1 = g_1 \mid g_0)} \quad (5)$$

Since $P(G_1=g_1|g_0)$ does not depend on d, the task reduces to maximize

$$P(G_1 = g_1 \mid d, g_0) P(d \mid g_0) \quad (6)$$

For a solution the probability distributions have to be known. They are specified by formulating appropriate models.

3.3. *Model of motion*

First a model to derive the probability $P(G_1=g_1|d,g_0)$ is proposed.
For the true underlying image u pixel intensities along the motion trajectories are assumed.to be costant:

$$u_0(\vec{x}) = u_1(\vec{x} + \vec{d}) \quad (7)$$

The observed images g are derived from u with a measuring process and thus noise is added to the pictures. Furthermore transformations, like filtering and discretisation on a grid, are applied.
To extend the model of constant pixel intensities to the observed images displaced pixel differences are defined:

$$r(\vec{d}(\vec{x}_i),\vec{x}_i) = g_1(\vec{x}_i+\vec{d}(\vec{x}_i)) - g_o(\vec{x}_i) \quad (8)$$

The continuous displacement vectors d usually do not end in grid points, so values for g have to be calculated by interpolation.

Equation (7) then can be extrapolated to observed images g by modelling the displaced pixel differences as independent Gaussian random variable with mean value 0:

$$P(r) \approx e^{-r/2\sigma^2}, \quad (9)$$

i.e. there is a high probability for small differences between $g_1(x_i+d(x_i))$ and $g_o(x_i)$.

Fixing image g_o and the displacement field d one obtains by using Eq. (7) and Eq. (8) the conditional probability of getting image g_1 when applying the vector field d to image g_o:

$$P(G_1 = g_1 \mid d, g_0) = c_1 e^{-U_g/2\sigma^2} \quad (10)$$

Here c_1 is a normalisation constant and the energy U is defined as the sum over all displaced pixel differences:

$$U_g = \sum_i (r(\vec{d}(x_i), x_i))^2 \quad (11)$$

Thus image g_1 is a probable realisation of G_1 when differences between $g_1(x_i+d(x_i))$ and $g_o(x_i)$ are small for all gridpoints.

Adding the assumption of constant pixel gradients along motion trajectories we define:

$$r_{grad}(\vec{d}(\vec{x}_i),\vec{x}_i) = grad(g_1(\vec{x}_i+\vec{d}(\vec{x}_i))) - grad(g_o(\vec{x}_i)) \quad (12)$$

analogous to r.

Using the same arguments as above we finally obtain:

$$P(G_1 = g_1 \mid d, g_0) = c_2 e^{-U_g/2\sigma^2 - U_{grad}/2\sigma^2_{grad}} \quad (13)$$

with c_2 being a normalisation constant and

$$U_{grad} = \sum_i (r_{grad}(\vec{d}(x_i), x_i))^2. \quad (14)$$

If the values $g_1(x_i+d(x_i))$ and *grad* $g_1(x_i+d(x_i))$ have only a small difference to $g_o(x_i)$ respectivly. *grad* $g_o(x_i)$, the energy functions U_g and U_{grad} are small also and the conditional probability $P(G_1=g_1|d,g_0)$ is high.

After the formulation of the model for $P(G_1=g_1|d,g_0)$, now the probability $P(D=d \mid g_o)$ has to determined. As a single image contributes little information to motion this information is omitted and just properties of the motion vector field are considered to calculate $P(D=d \mid g_o)$.

As cloud motion is caused by the rather smooth field above the atmospheric surface layer it is reasonable to assume also smooth motion vector fields, i.e. neighbouring vectors should not differ much from each other in direction and length.

This condition is used to model $P(D=d \mid g_o)$. Konrad and Dubois [8] applied the theory of Markov Random Fields tand showed that this approach leads to:

$$P(D = d \mid g_0) = c_3 e^{-U_d/\beta} \quad (15)$$

where c_3 is a normalisation constant β a constant characterising properties of the motion field and U_d is defined as:

$$U_d = \sum_{i,j \in N} \left\| \vec{d}(\vec{x}_i) - \vec{d}(\vec{x}_j) \right\|^2, \quad (16)$$

where $d(x_i)$ and $d(x_j)$ are neighbouring vectors.

A displacement vector field with large differences between neighbouring vectors thus has a high energy and is not a very probable one (Eq.(15)).

As now the two terms of Equation (6) are specified we find for the conditional probability for a vector field at given images g_o and g_1:

$$P(D = d \mid g_0, g_1) = \frac{1}{Z} e^{-U}, \quad (17)$$

where Z is a normalisation constant and U is defined as:

$$U = \lambda_1 U_g + \lambda_2 U_{grad} + \lambda_3 U_d. \quad (18)$$

The parameters $\lambda_1=1/2\sigma$, $\lambda_2=1/2\sigma_{grad}$ and $\lambda_3=1/\beta$ are weighting the contributions of the different energy functions to U. The determination of these parameters is discussed in section 3.4.

The maximum probability according to Equation (6) now can be found by determining the minimum of U.

3.4. *Simulated Annealing*

To find the minimum energy U Konrad and Dubois proposed the use of simulted annealing, a statistical method based on the analogy with the process of annealing solids. In analogy to the temperature in chemical annealing, the probabilty function is extended by a ”temperature “ parameter T:

$$P(D = d \mid g_o, g_1) = \frac{1}{Z} e^{-U/T} \quad (19)$$

T is decreasing exponentially to:

$$T_k = T_0 e^{-ak} \quad (20)$$

at iteration k

In order to find the minimum energy an initial vector field is chosen, all vectors are 0, and the following steps are repeated until the minimum is reached:

1) One vector is chosen randomly
2) The vector is chosen randomly
3a) If

$$P(D = d_{new} \mid g_o, g_1) > P(D = d_{old} \mid g_0, g_1) \quad (21)$$

the new vector is accepted.

3b) If

$$P(D = d_{new} \mid g_o, g_1) < P(D = d_{old} \mid g_0, g_1) \quad (22)$$

the new vector is accepted with the probability:

$$P(D = d_{new} \mid d_{old}, g_o, g_1) = \frac{1}{Z} e^{-(U_{new}-U_{old})/T} \quad (23)$$

A new vector can be accepted even if it is less probable than the previous one (step 3b). This allows the algorithm to escape local minima. For high temperatures, the probability to accept a less probable vector is also quite high: This is a good strategy, when the search algorithm starts and the energy is likely to be

in a local minimum. For very small temperatures the probability of accepting a less probable vector is approaching zero. This ensures that a global minimum once it is found is not left. Thus if T_0 is chosen to high, the algorithm converges very slowly, if T_0 is to small, it can be trapped in a local minimum. This can also happen if the temperature is decreasing to quickly, i.e. if a is to large. The choice of parameters thus is an important point when applying simulated annealing for minimisation.

3.4. *Determining model parameters*

To implement the method described above, we first have to fix the parameters, one the one hand for the model of motion and on the other hand for the minimisation routine. The values were determined by applying the routine for detection of motion on a typical cloudindex image and varying the parameters. A combination of parameters, which gave good results in a reasonable computing time, was chosen for the further application.

For the model of motion there are the weighting parameters λ_1,λ_2 and λ_3 of the energy function U (see Eq. (18)) and the number of vectors N, determining the resolution of the vector field. As we want to minimise U , it is enough to determine the ratios λ_1/λ_2 and λ_1/λ_3 which were chosen as $\lambda_1/\lambda_2 = 1$ and λ_1/λ_3. = 30. For the resolution of the vector field 1 vector for 5x5 pixels up to 10x10 pixels was found to be a good choice.

The model parameters for simulated annealing, the initial temperature T_0, the rate of decreasing the temperature a and the number of iterations (one iteration: N x step(1)-(3) from section3.4) until the energy minimum is (assumed to be) reached, where fixed as $T_0 = 30$, a=0.001 and n=6000.

3.5. *Forecasting with Motion Vector Fields*

To forecast the cloud situation of an image g_2, we first determine the motion of clouds using the previous images g_0 and g_1. As the wind field, which is responsible for cloud movement changes slowly with time, we assume that the motion vectors stay the same from image g_1 to g_2. Thus the motion vector field calculated from g_0 and g_1 can be applied on image g_1 to determine the future image g_2:

$$g_2(\vec{x}_i + \vec{d}(\vec{x}_i)) = g_1(\vec{x}_i) \tag{24}$$

To detect the Motion Vector Field we made the assumption that pixel intensities are constant along motion trajectories. In real situations the cloud reflectivity is changing with time: To take into account this effect, we record the change in intensity from image g_0 to g_1, the displaced pixel difference r (see Eq. (8)). Assuming that this tendency stays the same in future we add r to the value calculated with Eq.(24) and obtain:

$$g_2(\vec{x}_i + \vec{d}(\vec{x}_i)) = g_1(\vec{x}_i) + (g_1(\vec{x}_i) - g_0(\vec{x}_i - \vec{d}(\vec{x}_i)) \tag{25}$$

for the future cloudindex image.

4. RESULTS

4.1. *Test situations*

As a first check of the motion detection algorithm it is applied to artificial motion sequences with known motion patterns.

Fist we investigated the simplest case, translation with a constant vector all over the image. One test cloud index image g_0 is translated 8 pixels north and west to get image g_1. This is represented by the calcultaded motion vectors, as shown in Figure3.

To quantify the quality of the motion vectors image $g_{1'}$, obtained by applying the motion vector field on image g_0, is compared with the actual image g_1. The matching error between g_1 and $g_{1'}$ is given as the root mean square error:

$$rmse\_match' = \frac{1}{\sqrt{N}} \sqrt{\sum_i (g_1'(\vec{x}_i) - g_1(\vec{x}_i))^2} \tag{26}$$

The relative matching error is calculated by scaling the rmse'

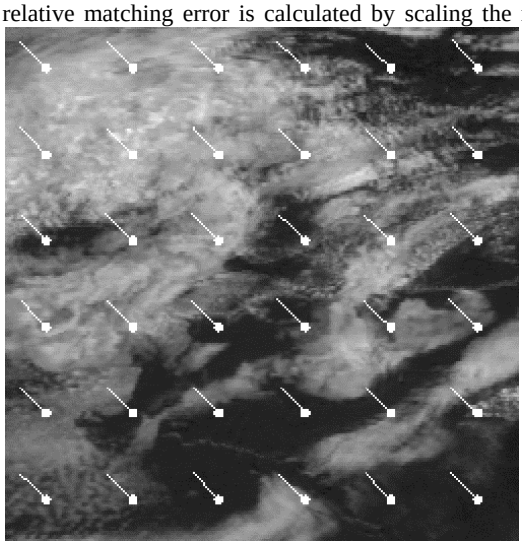

value with the mean pixel intensity of the image g=110.

Fig. 3. Cloudindex image (256x256 pixel) with translation vectors (6x6), dots represent foot points of vectors.

Already for a coarse resolution of only 6x6 vectors for an image of 256x256 pixels the relative root mean square error is very small: rms=3.8%.

To test the representation of rotational motion, the same test image was rotated counter clockwise by 5 degrees: To obtain good results a higher resolution of the vector field is required. Fig. 4 shows the resulting vector field for this type of motion. Only in the upper right corner, where a great variability in the cloud index image exists, the motion vectors do not represent the true motion.

The dependency of rms errors on the resolution of the vector field is shown in Table 1.

number of vectors	*rms error*
6 x 6	22 %
25 x 25	11 %
50 x 50	5 %

Table 1. Matching error for rotation of a test image by 5° with different resolutions of the vector field.

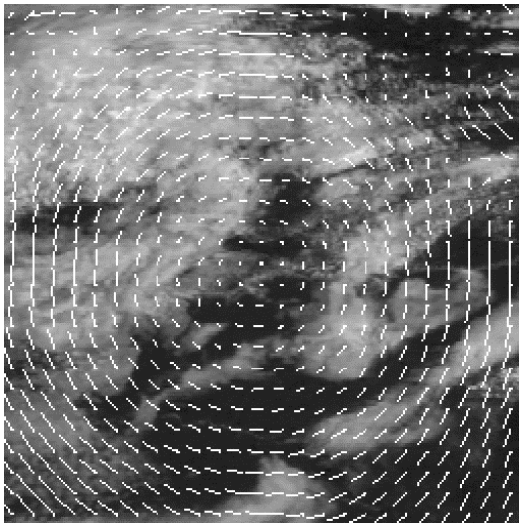

Fig. 4. Cloud index image (256x256 pixels) with vectors (25x25) calculated from 2 images rotated by 5° to each other.

4.2. *Influence of smoothness filter*

In section 2.3 the need to filter out the short scale variations of the images has been stated. After developing the routine for detection of motion, this effect now can be described quantitatively to choose the optimum filter size.
For all further calculations we used two time series : one, referred to as time series 1, of 50 days (10.4.1997 –29.5.1997) for northern Germany (100x65 pixel) and a second one time series 2 of 76 days (28.4.96 – 24.6.96) for Germany (256x256 pixel).
Binominal filters from size 1x1 pixel (i.e. no filter) to 19x19 pixel were applied to the images before and after the forecast. The results are shown in Fig. 5, where the mean forecast and mean matching error for time series 2 are plotted versus a filter parameter (filtersize: (2a+1)(2a+1) pixels).
The forecast error is again given as root mean square error between the forecasted image g_2' and the actual image g_2:

$$rms\_forec = \frac{1}{\sqrt{N}} \sqrt{\sum_i (g_1'(\vec{x}_i) - g_1(\vec{x}_i))^2} / g \qquad (27)$$

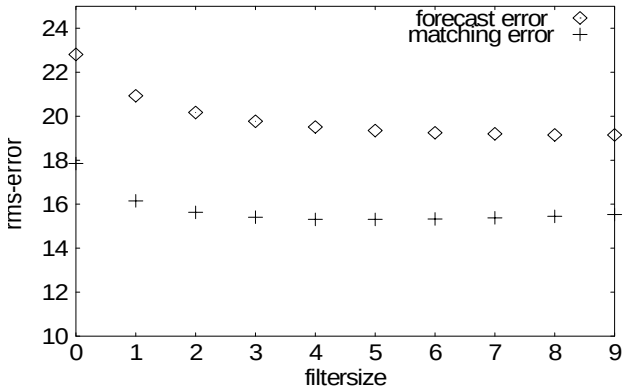

Fig 5. rms error depending on filtersize.

While the optimum filter size when looking at the matching error lies about a=5, the forecast error is still reducing slightly, when making the filter bigger.
This can be understand, when looking at the following effect: The motion vectors do not represent the motion perfectly and thus motion vectors might point to neighbouring pixels of the true ones. Hence taking into account these pixels for determining the new image, by applying a smoothing filter, makes the new image better. As the forecast error exceeds the matching error, this effect is bigger fore forecasting and thus the optimum filter size fore forecasting is higher than the best filter size due to the matching error.
As best filter size for forecasting we choose according to Fig. 5 19x19 pixels.

4.3. *Forecasting cloud index images*

An example for a motion vector field determined from two consecutive cloud images is given in Fig . 6
Fig. 7 shows the forecast error for a forecast horizon of 30 minutes for examples from 10 days from time series 1. For comparison also the error of persistence is plotted (persistence: future image = present image) .
It can be seen that the forecast error using motion vector fields, is always smaller than the persistence error. Especially for high persistence errors, the forecast errors are reduced considerably. For mean values derived from time series we get a forecast error of 18% compared to a mean persistence error of 25%. For time series 2 we get a reduction of the error from a persistence error of 27.% to forecast error of 19%
For a more detailed analysis of the forecast errors, in Fig 8 the forecast error is plotted as a function of the matching error (time series2). The forecast error has a strong correlation with the matching error, which indicates that the assumption of constant motion is reasonable. Errors in the Forecast errors are mainly caused by errors in determining the motion vectors for a forecast horizon of 30 minutes.
Fig. 9 shows the forecast error as a function of variability of the images, which is defined as the mean of the absolute values of pixel differences between neighbouring pixels.
While smooth images with low variability are easy to predict, images with a higher variability show significantly higher forecast errors.

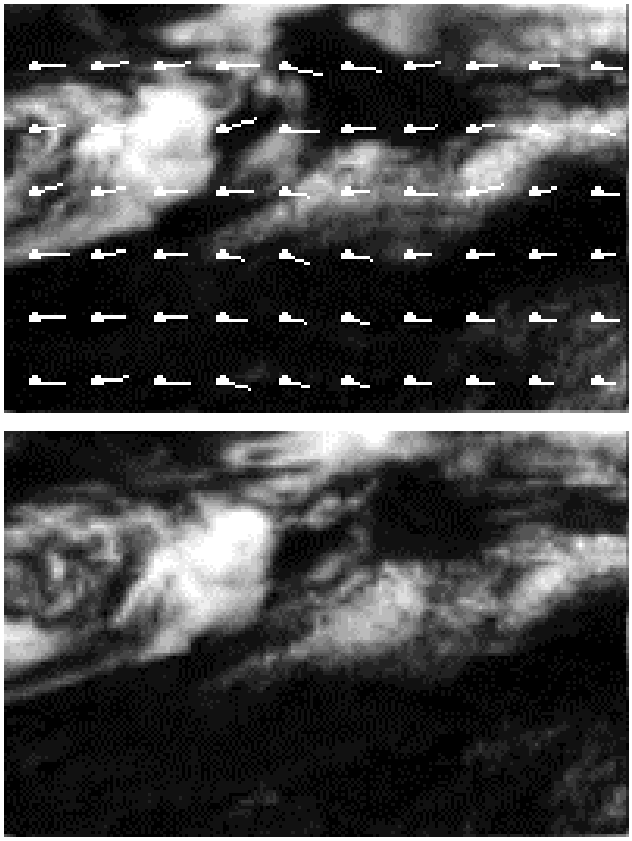

Fig. 6. Cloud images (100x65 pixel) with motion vectors determined from the two images.

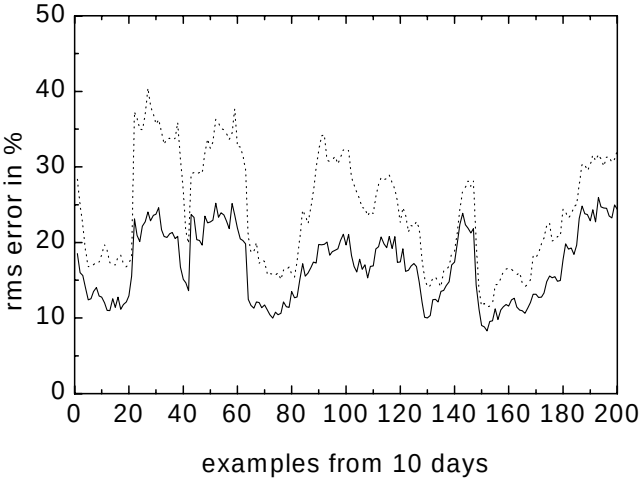

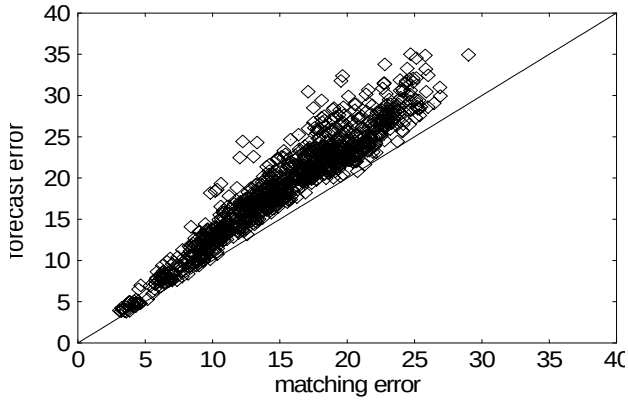

Fig. 7: Forecast (solid line) and persistence (dotted line) rms error for examples form times series 1 (10.4.1997 – 20.4.1997)

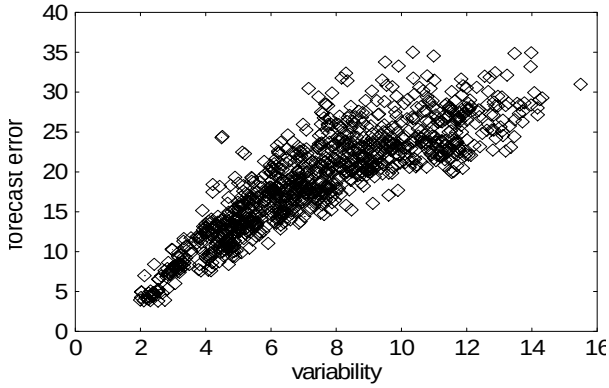

Fig. 8. Forecast error versus matching error (time series 2).

Fig. 9. Forecast error versus variability of the images (time series 2).

The forecast can be extended to larger forecast horizons by applying the calculated motion vector fields with a scaling factor on the present images. For forecast horizons larger than one hour the motion vector fields can also be determined from two images with a time lag of one hour between each other. The dependence of the forecast error on the forecast horizon is displayed in Fig. 10.The forecast based on the motion vectors for images with one hour time lag performs slightly worse than the forecast with 30 min motion vectors. Extending the forecast horizon from 30 min to 60 min the error of the forecast is increasing less than the persistence error. For more than one hour the difference between forecast and persistence stays almost constant at about 10% of mean pixel values.

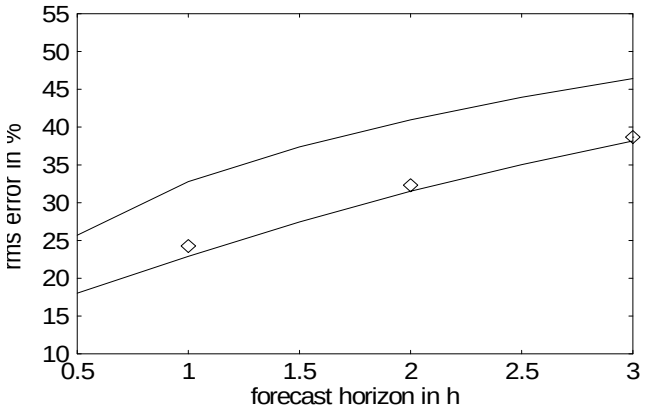

Fig. 10. Mean errors for forecast (bottom) and persistence (top) as a function of the forecast horizon for time series 1.

4.4. *Example: Forecast of the ensemble power output of photovoltaic systems*

As an example for the application of the forecasting algorithm, the power output of an ensemble of photovoltaic (PV) systems distributed over an area of 250 km x 250 km is estimated. This configuration shall represent the joint power production of PV in a regional utility grid.
The surface solar irradiance can be calculated using Eqn. (3):

$$G(\vec{x},t) = G_{clear}(\vec{x},t)(1-n(\vec{x},t)) \cdot \qquad (28)$$

As PV power can roughly be approximated to be linearly dependent on global irradiance, the following results are presented in terms of irradiance G instead of PV power. Also, optimum tilt angles are not considered here as they will have no influence on the spatial statistics of PV power generation.
Assuming a simple linear model for the photovoltaic generators and furthermore that all generators are the same, we get for the power output of an ensemble of N pv systems at time t:

$$P_{PV} = c\sum_{i=1}^{N} G(\vec{x}_i)(1-n(\vec{x}_i)) = cNG_{mean} \qquad (29)$$

The constant c reflects type and size of the PV systems and thus relates the ensemble mean irradiance G_{mean} and PV power.
As a measure of the forecast error we define

$$error\_forec(t) = abs(G_{mean}(t) - G_{mean,forec}(t)) \qquad (30)$$

The persistence error is defined in the same manner.
For an ensemble of 12 PV systems the daily pattern of G_{mean} is plotted in the upper graph of Figure 11. The lower graph shows forecast errors and persistence errors for the same time period. As expected the persistence error is generally higher than the forecast error. Especially maximum errors are significant reduced in the forecast (below 40 Wm^{-2}) as compared to persistence (up to 100 Wm^{-2}).
The errors for forecast and persistence show a daily pattern similar to irradiance G with maximum values around solar noon. The relative error error_forec/G_{mean} resulted not to depend on day time, the quality of the prediction of cloudindex values is the same all over the day.
The relative mean forecast and persistence error

$$\Delta G_{rel} = \frac{\sum_i error\_forec(t_i)}{\sum_i G_{mean}(t_i)} \qquad (31)$$

is shown in Fig. 12 for a varying number of PV systems. Different realisations for small ensembles with the same number of systems show statistical variations in the error due to the short time series used.

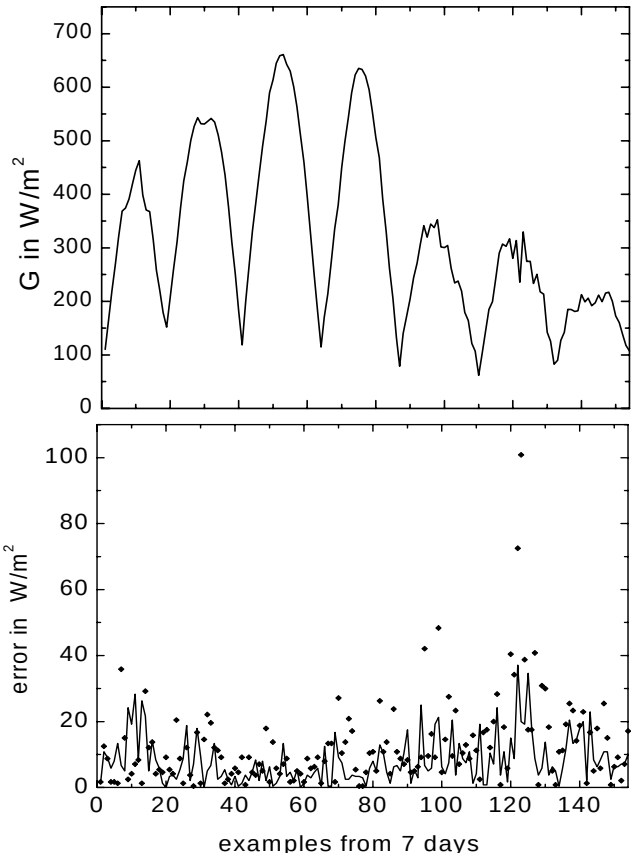

Fig. 11. Ensemble mean irradiance (top) and corresponding forecast (bottom, solid) and persistence errors (bottom, dots) for 12 spatially distributed PV systems. The time series includes daytime values only (7 days from time series 1). The forecast horizon is 30 minutes.

As expected, the forecast quality increases with the ensemble size. For large ensembles (>50 systems) forecasting (ΔG_{rel} = 3 %) gives only slightly better results than persistence (ΔG_{rel} = 4 %) and short-term forecasts of PV output are accurate with both methods. For small ensemble sizes the persistence error is reduced considerably using the forecast routine. Already for ensembles of 5 PV systems only, a mean error of 5 % is reached.

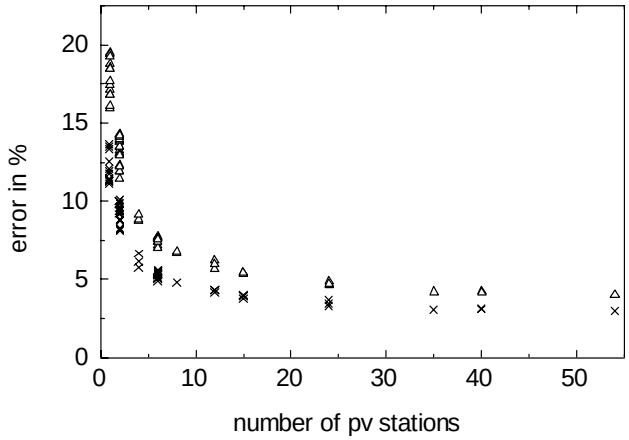

Fig. 12. Relative mean errors for forecasts (x) and persistence (Δ) as a function of the ensemble size (time series 1, forecast horizon 1h).

REFERENCES

(The references here are enclosed to serve as an example of Reference formatting in various cases)

Journal Article:
Feugard D. C., Abner R., Smith P. and Wayland D. (1994). Modelling daylight illuminance. *J. Climate Appl. Meterol.* 23, 93-109.

Journal Article in Press:
Feugard D. C., Abner R., Smith P. and Wayland D. Modelling daylight illuminance. *J. Climate Appl. Meterol.* In Press.

Book:
Duffie J. A. and Beckman W. A. (1991*) Solar Engineering of Thermal Processes*, 2n^{d} edn, pp.54-59. Wiley Interscience, New York.

Chapter in Edited Work:
Marcus B. C. and Nemo A. (1992) Estimation of total solar radiation from cloudiness in Spain. *In Global Solar Radiation*, Winchester F., Yu S., Pfaff S. W. and Major K. (eds), Vol 2, pp. 1393-1399. Raven Press, New York.

Page(s) in a Proceedings:
Weber D. J. and Hess W. M. (1985) Simple solar model for direct and diffuse irradiance. *In Proceedings of ISES Solar World Congres*s, 22-29 June, Montreal, Canada, Bilgen E. an Hollands K. G. T. (Eds), pp. 123-132, Pergamon Press, New York.